applied sciences

MDPI

Article

Research on Permanent Magnet Synchronous Motor Sensorless Control System Based on Integral Backstepping Controller and Enhanced Linear Extended State Observer

Lihuan Shao, Changfeng Zheng, Yan Zhang, Guanling Xie, Xiyu Hao and Xiaolong Zheng *

College of Electronic and Information, Hangzhou Dianzi University, Hangzhou 310018, China
* Correspondence: xlzheng@hdu.edu.cn

Abstract: The traditional sensorless control system of permanent magnet synchronous motor (PMSM) has the problems of low estimation accuracy and poor anti-interference ability. Moreover, the position estimation performance is subjected to position harmonic ripples caused by inverter nonlinearities and flux spatial harmonics. To optimize the dynamic performance of the PMSM sensorless control system, this paper proposes a sensorless control scheme that combines integral backstepping control with enhanced linear extended state observer (ELESO). The ELESO consists of two linear extended state observers (LESOs), which estimate the internal and external disturbances of the system, to improve the estimation accuracy of rotor position. Then, the integral backstepping controller processes the estimated rotor position and speed information to obtain d and q-axis voltages. The sensorless control scheme is implemented in the Matlab/Simulink and verified by experiments. The simulation and experiment show that the scheme can effectively suppress load interference and improve control accuracy.

Keywords: permanent magnet synchronous motor; sensorless control; integral backstepping control; enhanced linear extended state observer; rotor position estimation

Citation: Shao, L.; Zheng, C.; Zhang, Y.; Xie, G.; Hao, X.; Zheng, X. Research on Permanent Magnet Synchronous Motor Sensorless Control System Based on Integral Backstepping Controller and Enhanced Linear Extended State Observer. *Appl. Sci.* **2023**, *13*, 1680. https://doi.org/10.3390/app13031680

Academic Editors: Loránd Szabó and Feng Chai

Received: 6 December 2022
Revised: 25 January 2023
Accepted: 26 January 2023
Published: 28 January 2023

1. Introduction

Permanent magnet synchronous motors (PMSMs) adopt the field-oriented control (FOC) which have the advantages of small size, simple structure, high efficiency, large power density, and wide speed range. Therefore, PMSM can be widely used in aerospace, household appliances, and medical equipment fields [1]. To achieve efficient control of PMSM, a Hall sensor, optical encoder, and resolver are usually used to monitor the rotor position in time. However, this control scheme is highly dependent on the sensor, which increases the control cost. If the connection cable is too long, interference may be introduced into the system. In addition, working in high temperatures, low temperatures dirty air, and other environments will reduce the reliability of the system [2,3]. However, PMSM plays an important role in high-performance control places, so sensorless control technology came into being. The sensorless control technology discards the position sensor. By detecting the electrical signal in the motor winding, a certain control algorithm is used to estimate the rotor position and speed. Sensorless control represents the development trend of the three-phase PMSM control system. The core of sensorless control is the estimation of rotor position. Therefore, selecting an appropriate scheme to accurately estimate the real-time position of the PMSM rotor is an important part of sensorless control.

The sensorless rotor position acquisition of the PMSM mainly depends on the back electromotive force (EMF) estimation of the system [4]. As an effective position estimation method, the sliding-mode observer (SMO) has the advantages of a simple algorithm and strong robustness. In recent years, the SMO has been widely used in sensorless high-performance control of PMSM [5,6]. However, the switching function used by the traditional SMO has the problems of phase delay and speed chattering. Therefore, reducing

phase delay and speed chattering is a hot issue in SMO control. In Ref. [7], a new design of SMO was proposed to improve control accuracy. An observer is built according to the back EMF model after the back EMF equivalent signal is obtained. In this way, not only are low-pass filter and phase compensation modules eliminated but also estimation accuracy is improved. In Ref. [8], an SMO based on an adaptive super-twisting algorithm is proposed, in which the nonlinearity of the voltage source inverter (VSI) is considered. The algorithm reduces the error by compensating for the voltage distortion. Some schemes propose using the sigmoid function as a switching function to improve response speed and reduce chattering [9]. In addition, considering the double closed-loop module for processing the estimated parameters, the sliding mode controller (SMC) can replace the classical proportional-integral (PI) control algorithm. The SMC is insensitive to disturbances and parameters. In addition, it also has a fast response speed. Therefore, the SMC has been widely used in motor speed regulation systems and works with other control schemes [10–12]. In Ref. [13], a hybrid control strategy combining fuzzy SMC with load torque observer was proposed to accurately estimate load torque and suppress chattering. In Ref. [14], a fuzzy sliding mode speed controller for PMSM is proposed. The scheme combines the continuous terminal SMO, which can reach the balance point in a limited time to ensure the continuity of control and fast-tracking. Moreover, to improve the speed tracking accuracy, a neural network SMC scheme is proposed to optimize the control system [15].

Active disturbance rejection control (ADRC) has the advantages of strong anti-interference ability, weak model dependence, and a simple design process. Therefore, the ADRC has been successfully applied to motor drive systems. Extended state observer (ESO) is the core of ADRC, which was first proposed at the end of the 20th century [16]. The main idea of the ESO is to treat the unknown internal and external disturbances as the lumped disturbances of the system, thus expanding the disturbances into a new state variable [17]. Then, the new state variable can be estimated according to the output of the system. The ESO discards the low-pass filter and sliding mode function and improves the phase delay and chattering of the motor. Therefore, the ESO has extensive application prospects in motor control. In Ref. [18], a control strategy combining the ESO-based position estimation method and high-frequency current injection method was proposed. Compared with the traditional hybrid scheme, the two schemes were integrated into the same control structure, and the position observer was embedded in the current controller. The robustness of the control system is good in the full speed range. In Ref. [19], a linear active disturbance rejection controller (LADRC) design was proposed to reduce overshoot and improve dynamic response when a disturbance occurs. The ESO can effectively reduce the negative effects of phase delay and motor chattering. However, when the interference factors are caused by the system, the ESO cannot filter them out in time.

The SMC can solve the poor adaptability of the PI controller to external disturbances. However, when the state trajectory reaches the sliding mode surface, it is difficult to slide strictly along the sliding mode to the equilibrium point, resulting in chattering. In Ref. [20], using the saturation function instead of the switching function can effectively attenuate chattering. However, the traditional reaching law is difficult to suppress chattering and keep the system stable at the origin. The backstepping control considers both the control law and the adaptive law, which can make the whole closed-loop system meet the desired dynamic and static performance. Therefore, many scholars began to study the double closed-loop control based on the backstepping method to obtain a good load disturbance suppression effect. Different from the conventional feedback control methods, the backstepping control is a cascade design method. The controller aims to decompose the complex system into subsystems that do not exceed the system order. The controller designs the state variables and the Lyapunov functions for each subsystem so that the local and global stability characteristics run through each step [21]. In general, the backstepping controller makes the control process systematic and structured through reverse design. However, keeping the convergence of backstepping control and eliminating the steady-state error still needs to be concerned when the system parameters contain uncertainties.

To solve the above problems, this paper proposes a control scheme that combines an integral backstepping controller with an enhanced linear extended state observer (ELESO). Firstly, the ELESO is composed of two linear extended state observers (LESOs) cascaded, which estimate the rotor lumped interference and the internal interference of the system to eliminate the influence of the higher harmonics on position estimation. Secondly, the new Lyapunov functions are designed by adding integral terms to the backstepping controller. The integral backstepping controller can guarantee convergence and eliminate steady-state error. Moreover, the parameters of PMSM can be estimated by backstepping controller to further eliminate the internal disturbance. Finally, the effectiveness of the control algorithm is proved by simulation and experiment. The remainder of this paper is organized as follows. In Section 2, the ELESO and the integral backstepping controller are designed. In Section 3, the improved control algorithm is verified by simulation and experiment, and the results are analyzed. Finally, in Section 4, the research contents are summarized.

2. Theoretical Analysis of the Integral Backstepping Controller and the ELESO

This section will give the classical mathematical model of PMSM and important transformation formulas. The ELESO and the backstepping controller are designed according to the reference model.

2.1. The Mode of PMSM

To simplify the mathematical model of the three-phase PMSM in the natural coordinate system, the coordinate transformation includes static coordinate transformation (Clark transformation) and synchronous rotation coordinate transformation (Park transformation) [22]. After the Clark transformation and the Park transformation, the mathematical model of PMSM in the d-q synchronous rotation coordinate system is shown as follows [23]:

$$\begin{cases} \frac{di_d}{dt} = -\frac{R_S}{L_d} i_d + \frac{L_q}{L_d} n_p \omega i_q + \frac{1}{L_d} u_d \\ \frac{di_q}{dt} = -\frac{R_S}{L_q} i_q - \frac{L_d}{L_q} n_p \omega i_d - \frac{\psi_f n_p}{L_q} \omega + \frac{1}{L_q} u_q \\ \frac{d\omega}{dt} = \frac{3}{2} \frac{n_p}{J} \left(\psi_f i_q + (L_d - L_q) i_d i_q \right) - \frac{1}{J} T_L - \frac{B}{J} \omega \\ \frac{d\theta_e}{dt} = n_p \omega \end{cases} \tag{1}$$

where u_d, u_q are the stator voltages of the d and q-axis. i_d, i_q are the stator currents. R_s is the stator resistance. L_d, L_q are d and q-axis inductances. ω is the mechanical angular speed of the rotor. J is rotor inertia. B is the viscous friction coefficient. n_p is the number of pole pairs. ψ_f is the magnetic flux of the permanent magnet. T_L is the load torque.

2.2. Design of ELESO

In the static coordinate system, the voltage equation of salient pole PMSM is as follows:

$$\begin{bmatrix} u_\alpha \\ u_\beta \end{bmatrix} = \begin{bmatrix} R_s + pL_d & \omega_e(L_d - L_q) \\ -\omega_e(L_d - L_q) & R_s + pL_d \end{bmatrix} \begin{bmatrix} i_\alpha \\ i_\beta \end{bmatrix} + \begin{bmatrix} E_\alpha \\ E_\beta \end{bmatrix} \tag{2}$$

where u_α and u_β are the stator voltages in the static coordinate system. i_α and i_β are α and β-axis stator currents. $\omega_e = n_p\omega$ is the rotor's electrical angular speed. L_α, L_β are the stator inductance. p is the differential operator. E_α and E_β are the extended back EMF, which can be expressed as follows:

$$\begin{bmatrix} E_\alpha \\ E_\beta \end{bmatrix} = \left(\omega_e \left[(L_d - L_q) i_d + \psi_f \right] - (L_d - L_q) p i_q \right) \begin{bmatrix} -\sin\theta_e \\ \cos\theta_e \end{bmatrix} \tag{3}$$

It can be seen from Equation (3) that the extended back EMF contains rotor position information. Therefore, the estimation of back EMF in static coordinates will directly affect the estimation accuracy of the rotor position.

The ESO can estimate the lumped disturbance of the system accurately and efficiently. The basic form of the second-order LESO is expressed as:

$$\begin{cases} \varepsilon = z_1 - x_1 \\ \dot{z}_1 = z_2 + f + b_0 u - \beta_1 \varepsilon \\ \dot{z}_2 = -\beta_2 \varepsilon \end{cases} \tag{4}$$

where ε is the estimated error. x_1 is the actual state variable. z_1 is the estimation of x_1. z_2 is the estimated disturbance. u is the system input. f is the known disturbance, which contains the known model information of the system. b_0 is the system parameter. β_1 and β_2 are the observer gains. If the α and β-axis back EMF components with non-ideal conditions are considered as external interference, the state equation of stator current is as follows:

$$pi_x = f_{e_x} + f_x + u_x / L_d, x = \alpha, \beta \tag{5}$$

where f_{e_x} represents the lumped interference of the system, which is the sum of the external interference and the internal interference. f_x represents known model information, which can be expressed as follows:

$$\begin{cases} f_\alpha = \hat{\omega}_e (L_q - L_d) i_\beta / L_d - R_s i_\alpha / L_d \\ f_\beta = \hat{\omega}_e (L_d - L_q) i_\alpha / L_d - R_s i_\beta / L_d \end{cases} \tag{6}$$

where $\hat{\omega}_e$ is the estimated value of rotor electrical angular speed. Then, according to the definition of the state equation, the external disturbance state observer LESO1 is designed as follows:

$$\begin{cases} \varepsilon_x = \hat{i}_x - i_x \\ p\hat{i}_x = \hat{f}_{e_x} + f_x + u_x / L_d - \beta_{x1} \varepsilon_x \\ p\hat{f}_{e_x} = -\beta_{x2} \varepsilon_x \end{cases} \tag{7}$$

where $\hat{i}_x$ is the estimated value of the current. β_{x1} and β_{x2} are the gains of the LESO1. According to Equations (2) and (5), the estimated back EMF is as follows:

$$\begin{bmatrix} \hat{e}_\alpha \\ \hat{e}_\beta \end{bmatrix} = -L_d \begin{bmatrix} \hat{f}_{e_\alpha} \\ \hat{f}_{e_\beta} \end{bmatrix} \tag{8}$$

Based on the estimated back EMF, the position and the speed of the rotor under sensorless conditions can be obtained through the phase-locked loop (PLL). However, in practice, the inverter nonlinearity will generate different 5th and 7th harmonics in the phase current. As a result, (6k + 1) subharmonics will appear in the back EMF estimation, which results in six harmonic fluctuations in the estimated rotor position and speed [24]. The sixth harmonic will reduce the performance of the control system. The back EMF formula including the sixth harmonic component is as follows:

$$\begin{cases} \hat{e}_\alpha = -E_{ex} \sin(\omega_e t + \theta_e) - E_{6k\pm1} \sin((6k+1)\omega_e t + \theta_{6k\pm1}) \\ \hat{e}_\beta = -E_{ex} \sin(\omega_e t + \theta_e) + E_{6k\pm1} \cos((6k+1)\omega_e t + \theta_{6k\pm1}) \end{cases} \tag{9}$$

The rotor angle estimation error becomes:

$$\varepsilon_\theta = \theta_e - \hat{\theta}_e + E_{6k} \sin(6k\omega_e t + \theta_{6k}) \tag{10}$$

where $E_{ex} = \omega_e \cdot \psi_f$. In general, there is only the harmonic effect when $k = 1$. Therefore, after the whole FOC control finishes, the output rotor angle error will contain the sixth harmonic component. The ADRC does not require an accurate motor model. According to this characteristic, this paper proposes an internal disturbance observer LESO2 to estimate the internal disturbance of the system. The LESO2 is cascaded with the LESO1. With this scheme, the influence of higher harmonics and motor parameter changes of the system

performance can be eliminated as far as possible. At this time, the stator current model is shown as follows:

$$pi_x = f_{e_x} + f_x + u_x/L_d + f_{e_{hx}}, x = \alpha, \beta \tag{11}$$

where $f_{e_{hx}}$ represents the internal disturbance in the static coordinate system, which is the high-order harmonic back EMF. According to the current formula, the LESO2 is designed as follows:

$$\begin{cases} \varepsilon_{hx} = \hat{i}_{hx} - i_x \\ p\hat{i}_{hx} = \hat{f}_{e_x} + f_x + \hat{f}_{e_{hx}} + u_x/L_d - \beta_{x3}\varepsilon_{hx} \\ p\hat{f}_{e_{hx}} = -\beta_{x4}\varepsilon_{hx} \end{cases} \tag{12}$$

where $\hat{i}_{hx}$ is the estimated current component under the higher harmonic. ε_{hx} is the estimation error. $\hat{f}_{e_{hx}}$ is the estimated internal disturbance. β_{x3} and β_{x4} are the gains of the LESO2.

According to Equations (3) and (8), the estimated rotor position can be calculated as:

$$\hat{\theta}_e = \arctan\left(\frac{-\hat{e}_\alpha}{\hat{e}_\beta}\right) \tag{13}$$

In Equation (13), the estimated rotor position can be obtained directly. However, the arctangent function is very sensitive to noise. The position extraction method based on the arctangent function directly brings this noise into the operation, which leads to the error being amplified, thus causing greater angle estimation error. This uncertainty will reduce the accuracy and stability of the control system, especially in the middle and low speed range. Therefore, it is necessary to use the PLL to extract speed and position information from the estimated back EMF [25].

β_{x1}, β_{x2}, β_{x3} and β_{x4} are the gains of the LESO1 and the LESO2. If the gains are not properly selected, it will lead to the loss of position in the process of controller evaluation, which will lead to system instability [26,27]. Therefore, the selection of gains is an important issue. Taking the LESO1 as an example, the tracking error is defined as follows:

$$e = \begin{bmatrix} \hat{i}_x - i_x \\ \hat{f}_{e_x} - f_{e_x} \end{bmatrix} \tag{14}$$

According to Equations (5) and (7), the error state equation can be derived as:

$$\dot{e} = C_m e, C_m = \begin{bmatrix} -\beta_{x1} & 1 \\ -\beta_{x2} & 0 \end{bmatrix} \tag{15}$$

Equation (15) shows that the eigenvalues of C_m determine the behavior of the LESO1. If and only if $\beta_{x2} > 0$, Equation (15) is asymptotically stable. Therefore, the gains of the LESO1 can be selected according to the bandwidth of the LESO1 [28]. Specifically, the gains of the LESO1 are designed such that C_m has a double eigenvalue λ that is equal to the bandwidth of the LESO1 [29]. The characteristic equation is as follows:

$$|\lambda E - C_m| = \begin{vmatrix} \lambda + \beta_{x1} & -1 \\ \beta_{x2} & \lambda \end{vmatrix} = \lambda^2 + \beta_{x1}\lambda + \beta_{x2} = (\lambda + \omega_0)^2 \tag{16}$$

where ω_0 is the bandwidth of the LESO1. ω_0 should be large enough to ensure that the system can respond quickly. According to ω_0, the gains of the LESO1 can be obtained as follows:

$$\beta_{x1} = 2\omega_0, \beta_{x2} = \omega_0^2 \tag{17}$$

The gains selection of the LESO2 is similar to the LESO1.

Figure 1 is the control diagram of the ELESO. u_x is the system input, which is represented as the voltage component in the static coordinate system in the PMSM control. i_x is the current component in the static coordinate system. f_x can be calculated by combining

motor parameters with dynamic components. The three inputs act on the LESO1 and the LESO2, respectively. By subtracting the internal interference from the lumped interference, the back EMF can be obtained in the static coordinate system with high-frequency harmonics filtered. According to the estimated back EMF, the rotor position and the speed are obtained in the PLL. This scheme eliminates the low-pass filter and discrete sliding mode function and improves the phase delay and chattering problems. The ELESO can obtain high-precision estimation parameters.

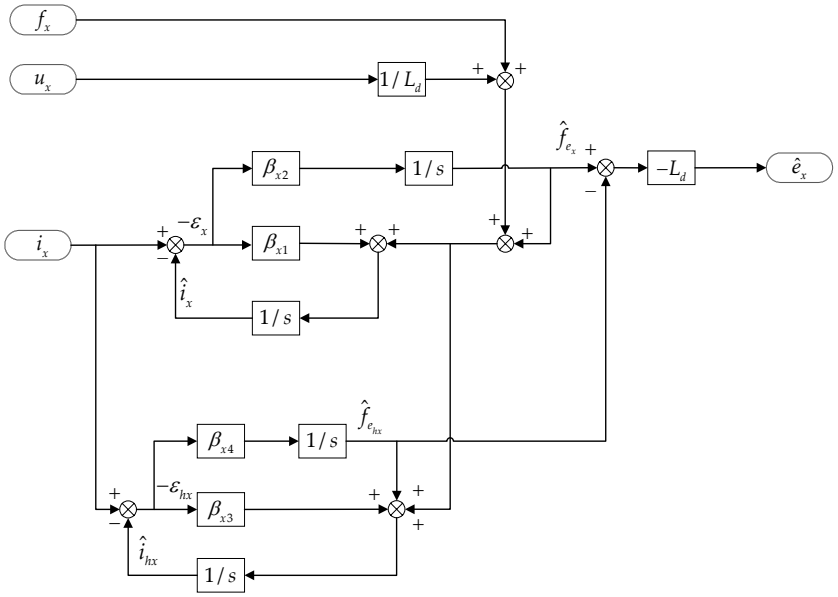

Figure 1. Block diagram of the plant controlled by the ELESO scheme.

2.3. Design of Backstepping Control

The backstepping control is used to decompose the complex nonlinear system into subsystems that do not exceed the system order, then design the corresponding Lyapunov function and intermediate virtual control quantity for each subsystem [30]. At each stage, the current Lyapunov function will be based on the state of the previous subsystem, including the current virtual control quantity to ensure system stability [31]. The control steps are mainly divided into the following steps: Firstly, the controller selects some states of the system as subsystems and designs the Lyapunov functions. According to the virtual control quantity of the subsystem, the virtual error variable is designed. A new subsystem is composed of the virtual error variable and the previous subsystem. A new Lyapunov function is designed to stabilize the new system. If the actual control quantity of the system is not obtained, the subsystem shall be designed recursively. Otherwise, the actual control quantity shall be designed to stabilize the whole system [32]. Each new system is designed on the premise that its subsystems are stable, so that the final control system can be stable.

According to the estimated position and the estimated speed of the rotor obtained by the ELESO, this paper proposes an integral backstepping control module with a speed controller and current controller cascaded. The reference values of rotor speed and d and q-axis currents are defined as ω_r, i_{dref} and i_{qref}. First, for the speed loop with a given reference speed, assuming that the control target of the system is speed tracking. Tracking error is constructed as follows:

$$e_\omega = \omega_r - \omega + e_{\omega I} \tag{18}$$

where $e_{\omega I}$ is the integral of the estimation error in the sampling time. This term is added to ensure that the system can converge even if the system parameters contain uncertainties. $e_{\omega I}$ is expressed as follows:

$$e_{\omega I} = K_\omega \int_0^t (\omega_r - \omega) dt \tag{19}$$

To make the speed tracking error approaches zero, i_{qref} is designed as a virtual control variable. The candidate Lyapunov function is constructed as follows:

$$V_\omega = \frac{1}{2} e_\omega^2 \tag{20}$$

The derivative of e_ω can be obtained by combining Equations (1) and (18):

$$\dot{e}_\omega = \dot{\omega}_r - \frac{3}{2}\frac{n_p}{J}\left(\psi_f i_{qref} + (L_d - L_q) i_d i_{qref}\right) + \frac{1}{J} T_L + \frac{B}{J}\omega + K_\omega(\omega_r - \omega) \tag{21}$$

Then, the derivative of the candidate Lyapunov function shown in Equation (20) is:

$$\dot{V}_\omega = e_\omega \dot{e}_\omega = e_\omega \left[\dot{\omega}_r - \frac{3}{2}\frac{n_p}{J}(\psi_f i_{qref} + (L_d - L_q) i_d i_{qref}) + \frac{1}{J} T_L + \frac{B}{J}\omega + K_\omega(\omega_r - \omega)\right] \tag{22}$$

To make Equation (22) negative definite, i_{qref} is taken as follows:

$$i_{qref} = \frac{J}{\frac{3}{2} n_p (\psi_f + (L_d - L_q) i_d)} \left[K_1 e_\omega + \dot{\omega}_r + \frac{1}{J} T_L + \frac{B}{J}\omega + \dot{e}_{\omega I}\right] \tag{23}$$

The result of Equation (22) is as follows:

$$\dot{V}_\omega = -K_1 e_\omega^2, K_1 > 0 \tag{24}$$

T_L is used in Equation (23). T_L is unknown in most drive control designs. Therefore, it can be estimated according to the speed information obtained in the ELESO and Equation (1) [33].

At this time, the system has achieved the goal of global progressive speed tracking. To achieve complete decoupling and speed tracking of the PMSM, the current under the synchronous rotating coordinate system can be selected as follows:

$$\begin{cases} i_{qref} = \frac{J}{\frac{3}{2} n_p (\psi_f + (L_d - L_q) i_d)} \left[K_1 e_\omega + \dot{\omega}_r + \frac{1}{J} T_L + \frac{B}{J}\omega + \dot{e}_{\omega I}\right] \\ i_{dref} = 0 \end{cases} \tag{25}$$

The current tracking error is selected as the virtual control variable. The current error is defined as follows:

$$\begin{cases} e_q = i_{qref} - i_q + i_{qe} \\ e_d = i_{dref} - i_d + i_{de} \end{cases} \tag{26}$$

where i_{de} and i_{qe} are the integral terms, which are expressed as follows:

$$i_{xe} = K_x \int_0^t (i_{xref} - i_x) dt, x = d, q \tag{27}$$

At this time, a new system is being constructed. Consider the following candidate Lyapunov function:

$$V_q = V_\omega + \frac{1}{2} e_q^2 + \frac{1}{2} i_{qe}^2 \tag{28}$$

The derivative of Equation (28) can be obtained by combining Equations (1), (24) and (26):

$$\begin{aligned}\dot{V}_q = &-K_1 e_\omega^2 + e_q\left[\frac{di_{qref}}{dt} + \frac{R_S}{L_q} i_q + \frac{L_d}{L_q} n_p \omega i_d + \frac{\psi_f n_p}{L_q}\omega - \frac{1}{L_q} u_q + K_q(i_{qref} - i_q)\right] \\ &+ i_{qe} K_q (i_{qref} - i_q)\end{aligned} \tag{29}$$

According to Equation (29), the control quantity u_q is selected as follows:

$$u_q = L_q\left[K_2 e_q + \frac{di_{qref}}{dt} + \frac{R_S}{L_q} i_q + \frac{L_d}{L_q} n_p \omega i_d + \frac{\psi_f n_p}{L_q}\omega\right] \tag{30}$$

Substituting Equation (30) into Equation (29) yields:

$$\begin{aligned}\dot{V}_q &= -K_1 e_\omega^2 - K_2 e_q^2 + (e_q + i_{qe}) K_q (i_{qref} - i_q) \\ &= -K_1 e_\omega^2 - K_2 e_q^2 + (e_q + i_{qe}) K_q (e_q - i_{qe}) \\ &= -K_1 e_\omega^2 - (K_2 - K_q) e_q^2 - K_q i_{qe}^2\end{aligned} \tag{31}$$

The result of Equation (31) is as follows:

$$\dot{V}_q \le -K_Q V_q, K_Q = \min\{K_1; (K_2 - K_q); K_q\} \tag{32}$$

For the d-axis current i_d, the target $i_{dref} = 0$. The control value is u_d. Similar to the previous subsystem construction process, the candidate Lyapunov function is defined as:

$$V_d = \frac{1}{2} e_d^2 + \frac{1}{2} i_{de}^2 \tag{33}$$

The derivative of Equation (33) yields:

$$\begin{aligned}\dot{V}_d &= e_d\left(\frac{di_{ref}}{dt} - \frac{di_d}{dt} - K_d i_d\right) + i_{de} K_d (i_{dref} - i_d) \\ &= e_d\left(\frac{R_S}{L_d} i_d - \frac{L_q}{L_d} n_p \omega i_q - \frac{1}{L_d} u_d\right) + K_d (e_d + i_{de})(e_d - i_{de})\end{aligned} \tag{34}$$

According to Equation (34), the control quantity u_d is selected as follows:

$$u_d = L_d\left(K_3 e_d + \frac{R_S}{L_d} i_d - \frac{L_q}{L_d} n_p \omega i_q - \frac{1}{L_d} u_d\right) \tag{35}$$

Substituting Equation (35) into Equation (34) yields:

$$\dot{V}_d = -(K_3 - K_d) e_d^2 - K_d i_{de}^2 \tag{36}$$

Similar to Equation (32), $\dot{V}_d$ is represented as follows:

$$\dot{V}_d \le -K_D V_d, K_D = \min\{(K_3 - K_d); K_d\} \tag{37}$$

Through the design of the backstepping controllers, the speed controller and current controllers are cascaded to ensure that all virtual control variables will eventually converge to their reference values.

In practice, some parameters of the PMSM are not fixed. Its value changes over time. For example, the stator resistance will change as the temperature changes [34]. However, in sensorless control of using equation model, motor parameters such as resistance and inductance are used in calculation. The system operation is based on the assumption that these parameters are predetermined and conform to actual motor parameters. Therefore, the difference of motor parameters may affect the stability of the sensorless control system. To solve this problem, in [35], the author introduced the on-line parameter identification as a compensation method for motor parameter difference. Specifically, the Recursive Least

Squares method (RLS) is used as the core, and the appropriate forgetting matrix is selected to identify. The feasibility of the method is verified by simulation.

3. Simulation and Experimental Analysis

In this section, the PMSM sensorless control diagram based on the combination of the integral backstepping controller and the ELESO is shown in Figure 2. The ELESO calculates the estimated internal and external interference. The estimated rotor position and speed are obtained in PLL. D and q-axis voltages are obtained by the integral backstepping controller. After anti-Park transformation and SVPWM, the PWM signal is output to complete the whole control process. The experimental test platform is shown in Figure 3. Its components mainly include a PMSM, drive module, load, DC power supply, dynamic torque sensor, etc. The experiment uses STM32F407 chip and IR2110S driver chip as the core hardware platform to drive the 24 V on-board motor.

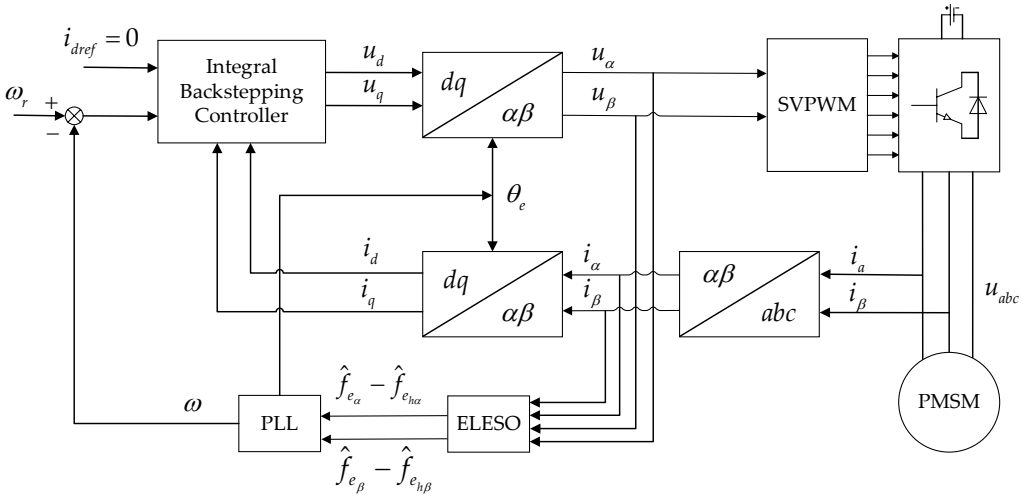

Figure 2. Block diagram of the scheme based on the integral backstepping controller and the ELESO.

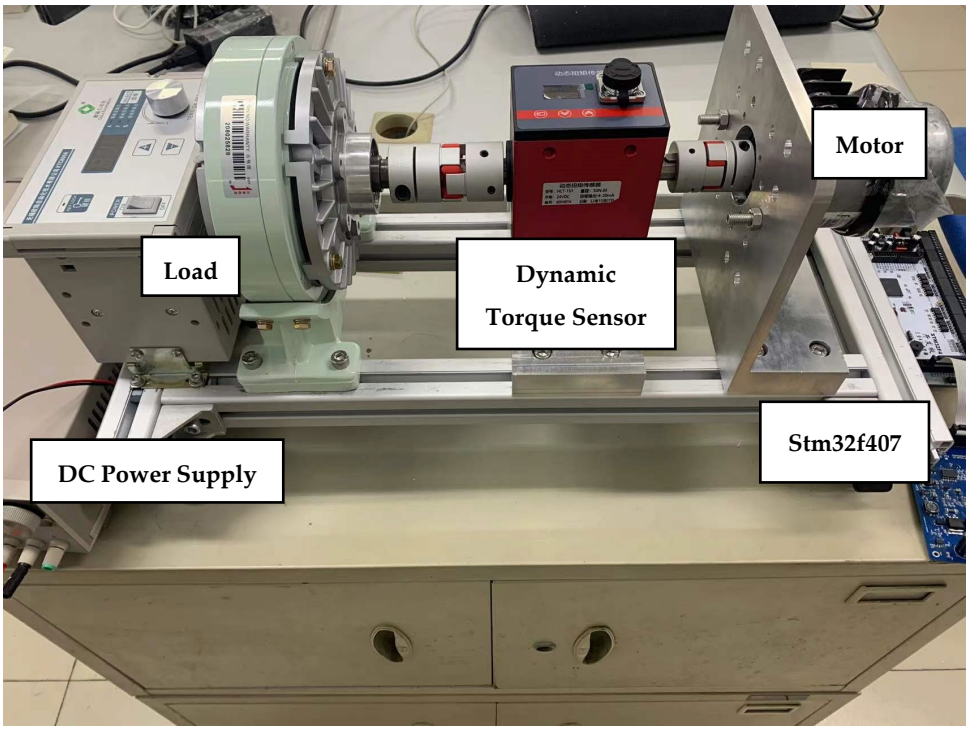

Figure 3. The experimental test platform.

3.1. Simulation Results and Analysis

Table 1 shows the parameters of the PMSM. According to the flow chart of the FOC control of PMSM, a simulation model is built in Matlab/Simulink for experimental verification. The backstepping controllers replace the traditional PI controllers and add an integral term to them. The ELESO obtains back EMF. In this paper, the control scheme combining the backstepping controller and the ESO is regarded as the old scheme, and the control scheme combining the integral backstepping controller and the ELESO is regarded as the new scheme. The new scheme is compared with the old scheme to verify the effectiveness of the new control scheme.

Table 1. PMSM parameters.

Parameters	Values
Stator resistance/Ω	1.5
Rated torque/N·m	6
d-axis inductance/mH	2.48
q-axis inductance/mH	2.95
Rated speed/rpm	1000
Moment of inertia/kg·m^2	0.0014
Flux linkage/wb	0.07
Viscous friction/B	7.2×10^{-4}
Pole pairs	4

According to the actual situation of the motor parameters, the characteristics of current tracking performance and anti-interference, the bandwidth of the LESO1 is selected as 500 Hz, and the bandwidth of the LESO2 is selected as 3000 Hz in the ELESO. In the backstepping controller, $K_1 = 4000$, $K_\omega = 200$, $K_2 = 13{,}000$, $K_q = 350$, $K_3 = 8000$, $k_d = 830$. Set the step size as 1×10^{-5} s. The motor accelerates from the static state to 500 rad/s. The rotor speed is raised to 1000 r/min at 0.5 s, and 6 N·m loads are applied to the rotor. Then, the motor runs at the rated speed.

Figure 4 shows the estimated back EMF under the old scheme. Due to the existence of harmonics, the estimated value of back EMF is not ideal. The influence of high-order harmonics on estimation accuracy is especially obvious at the low speed. According to the definition of the PLL and Equation (13), the back EMF information is finally converted into the estimated position information of the rotor. Therefore, this paper mainly shows the advantages of the new scheme from the position and speed of information.

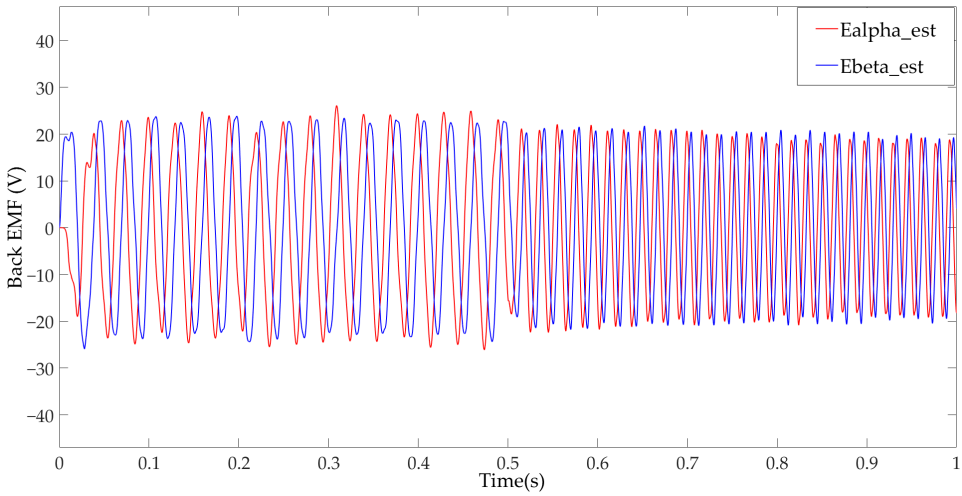

Figure 4. PMSM estimated back EMF of the control scheme of combining the backstepping controller with the ESO.

Figure 5 shows the PMSM three-phase current waveforms of the two control schemes under no-load startup. Comparing the two waveforms, it can be concluded that the scheme based on the integral backstepping controller and the ELESO has a higher sinusoidal current waveform because it filters out the higher harmonics.

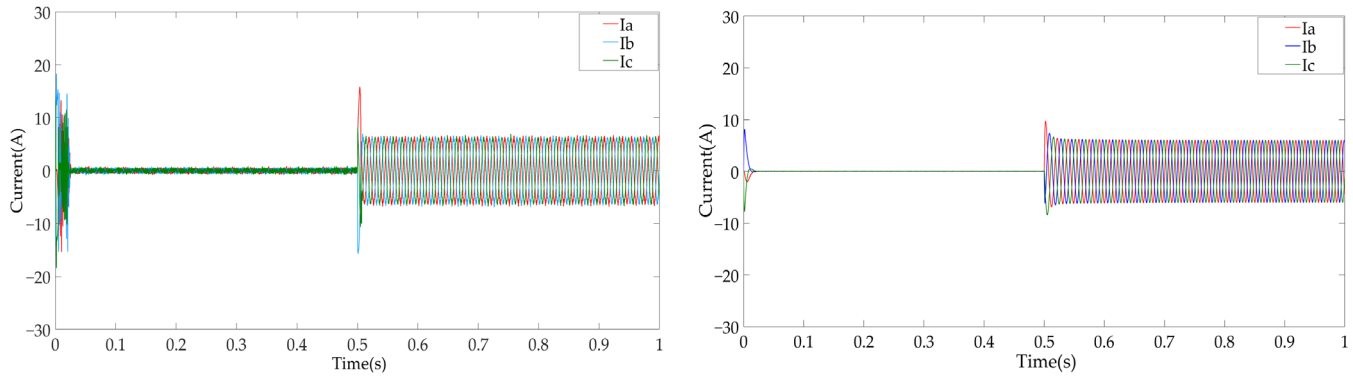

(**a**) (**b**)

Figure 5. PMSM stator three-phase current waveforms under no-load startup of the (**a**) Control scheme of combining the backstepping controller with the ESO and (**b**) Control Scheme of combining the integral backstepping controller with the ELESO.

Figure 6 shows the waveforms comparison between the estimated rotor position and the actual value under the two schemes. Combined with the rotor position error waveforms shown in Figure 7, it is obvious that the traditional scheme always has an estimation error of about 0.5 rad under no-load startup. The improved scheme will have fewer errors only at the moment of state change. With the stable operation of the motor, the position estimation error under the improved scheme is always stable at about 0 rad.

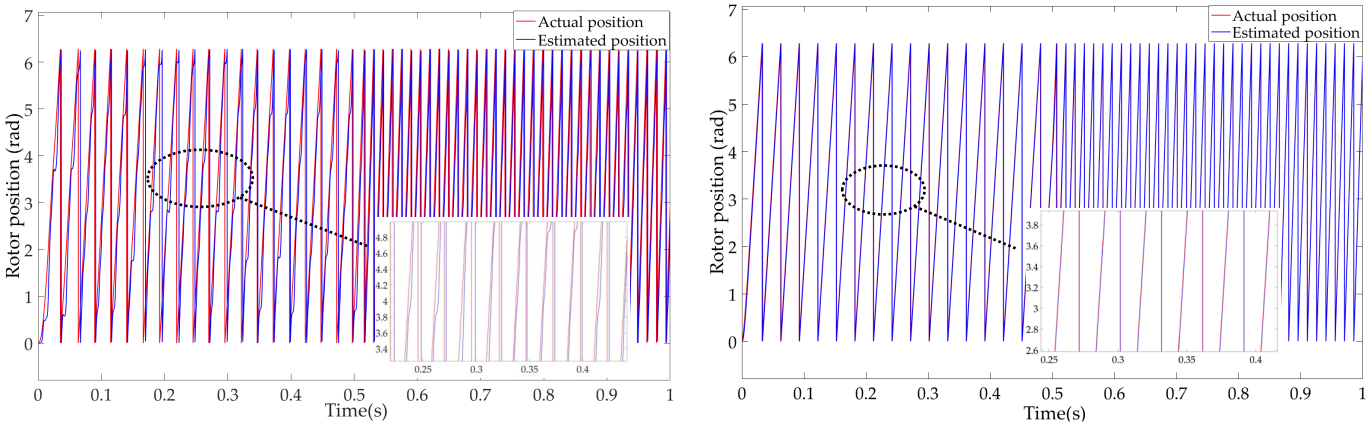

(**a**) (**b**)

Figure 6. PMSM rotor position tracking under no-load startup of the (**a**) Control scheme of combining the backstepping controller with the ESO and (**b**) Control Scheme of combining the integral backstepping controller with the ELESO.

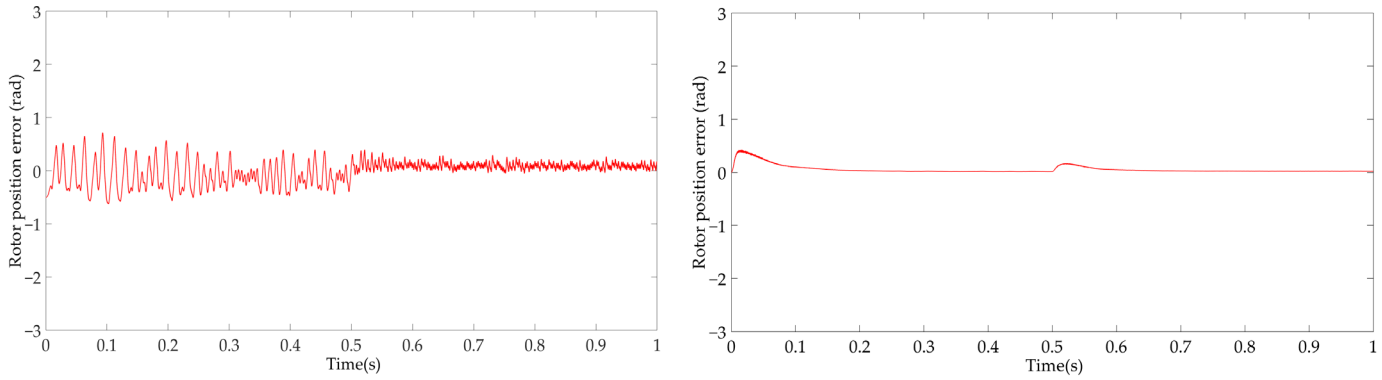

(**a**) (**b**)

Figure 7. PMSM rotor position tracking error under no-load startup of the (**a**) Control scheme of combining the backstepping controller with the ESO and (**b**) Control Scheme of combining the integral backstepping controller with the ELESO.

Figure 8 shows the d and q-axis currents of the two controllers. Due to the existence of higher harmonics, the waveforms in Figure 8a are not smooth. The high-order harmonics are filtered out in Figure 8b, so the d and q-axis currents are more stable. In addition, when the state changes in 0 s and 0.5 s, the jump amplitude of the current in Figure 8b is smaller.

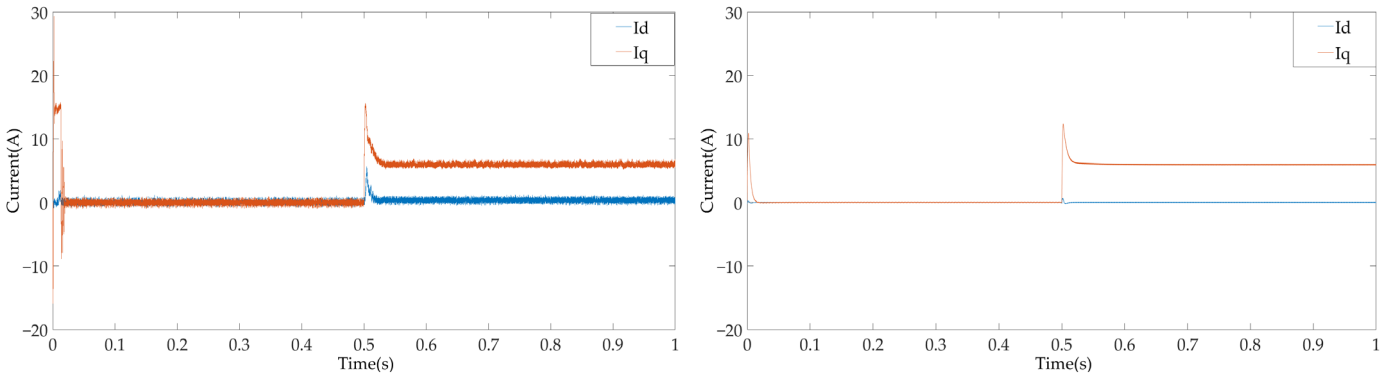

(**a**) (**b**)

Figure 8. PMSM d and q-axis currents under no-load startup of the (**a**) Control scheme of combining the backstepping controller with the ESO and (**b**) Control Scheme of combining the integral backstepping controller with the ELESO.

Figure 9 shows the rotor speed waveforms of the two controllers. The standard of rotor stability is that the rotor speed reaches the set value and can be stabilized around the set value. In Figure 9a, it takes about 0.07 s for the rotor speed to reach the set value. In Figure 9b, the waveform converges faster. The new scheme eliminates the influence of internal disturbances such as harmonic components and parameter changes. The speed waveform is smoother. The new scheme is more suitable for places with high requirements for motor speed accuracy.

According to the above waveforms, the control scheme of combining the traditional backstepping controller with the ESO does not eliminate the influence of the high-order harmonics and internal parameter changes of the motor. Therefore, the problem of jitter and poor sinusoidal performance will occur in this control scheme, especially at low speeds. The system always maintains an estimation error of about 0.5 rad, which affects the stable operation of the motor. Compared with the traditional scheme, the control scheme based on the integral backstepping controller and the ELESO has better tracking performance at a low speed. In the second stage of acceleration, the traditional control mode requires

0.06 s of reaction time, and the improved scheme only needs 0.01 s to reach the rated speed, which improves the reaction speed of the system.

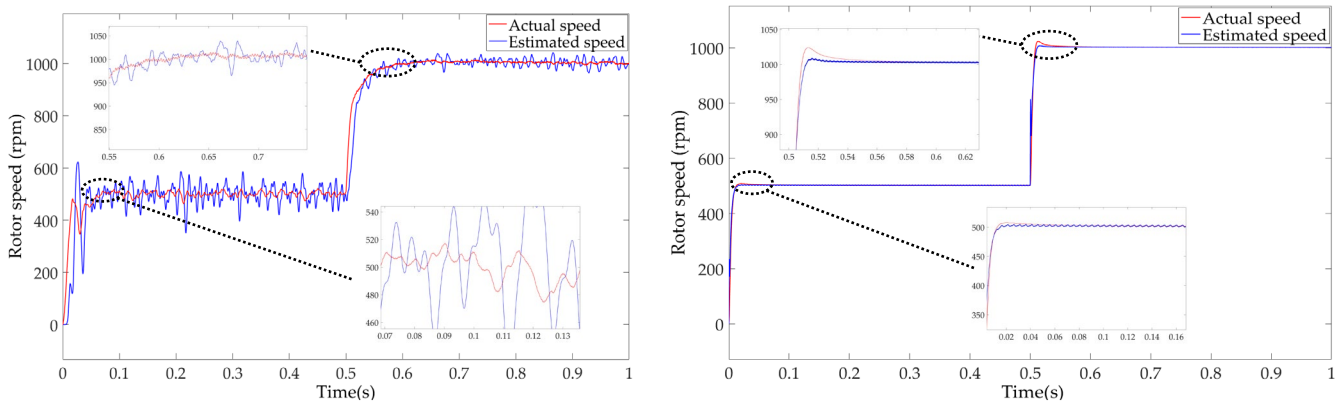

(**a**) (**b**)

Figure 9. PMSM rotor speed under no-load startup of the (**a**) Control scheme of combining the backstepping controller with the ESO and (**b**) Control Scheme of combining the integral backstepping controller with the ELESO.

The working principle of PMSM is that the magnetic field acts on the current force to make the motor rotate. When the motor is unloaded, the electromagnetic force is far greater than the force required for rotor rotation. When the motor is loaded, the resistance of the load on the rotor requires more force to rotate. Therefore, we need to conduct the motor on load starting test to verify whether the new scheme meets the expectations. Set the motor speed to the rated speed of 1000 r/min and the load to 6 N·m. The two methods are simulated, and the experimental results are analyzed.

Figure 10 shows the waveforms of the PMSM stator three-phase current under load startup test. Both schemes can obtain relatively stable three-phase waveforms under load startup, but the sinusoidal property of Figure 10a is worse than that of Figure 10b due to the existence of harmonics. In Figure 10b, the LESO2 timely estimated the harmonic components, and the external interference of the ELESO output no longer contains high-order harmonics, so the waveform is more sinusoidal.

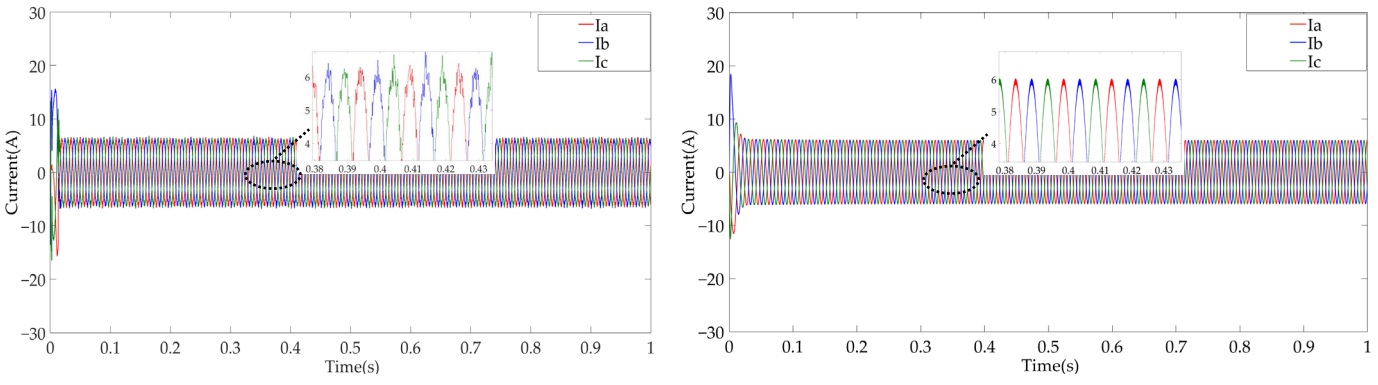

(**a**) (**b**)

Figure 10. PMSM stator three-phase current waveforms under load startup of the (**a**) Control scheme of the combining backstepping controller with the ESO and (**b**) Control Scheme of combining the integral backstepping controller with the ELESO.

Figure 11 shows the rotor position estimation waveforms under load startup. As shown in Figure 11, both control schemes can finally achieve the goal of real-time tracking.

According to the error waveforms shown in Figure 12, it can be obtained that the new scheme can converge faster. Compared with Figure 12a, the integral backstepping controller eliminates the steady-state error and further improves the system performance.

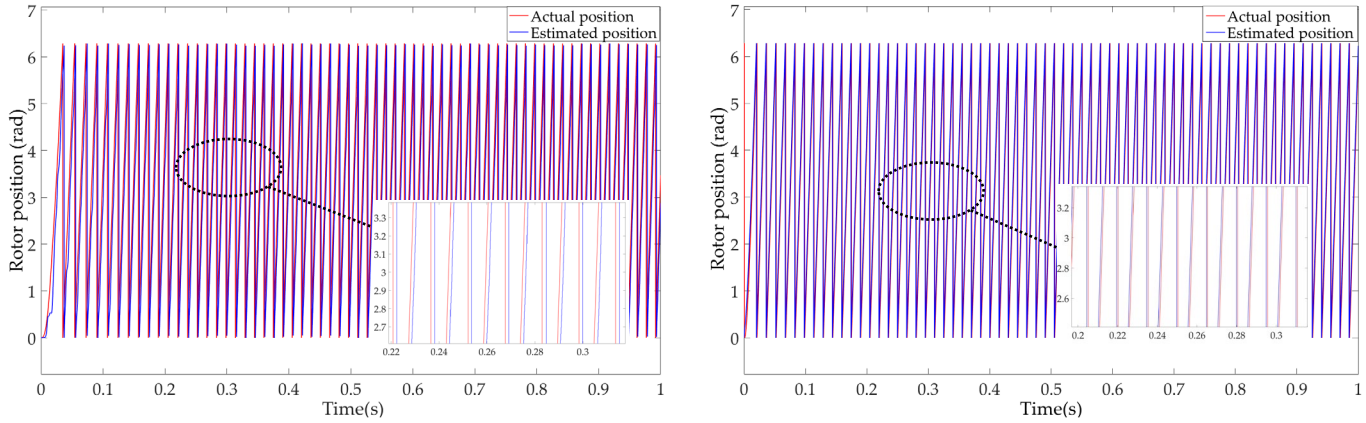

(**a**) (**b**)

Figure 11. PMSM rotor position tracking under load startup of the (**a**) Control scheme of combining the backstepping controller with the ESO and (**b**) Control Scheme of combining the integral backstepping controller with the ELESO.

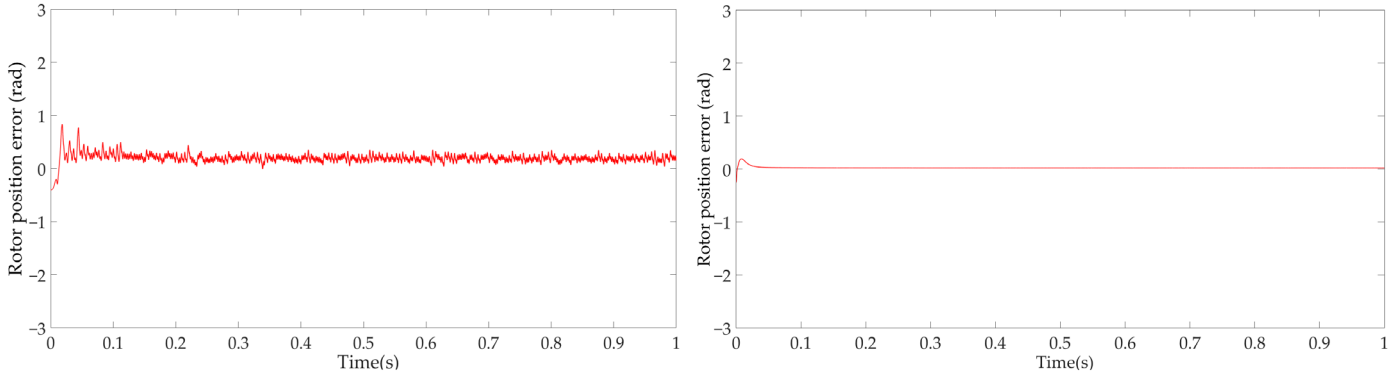

(**a**) (**b**)

Figure 12. PMSM rotor position tracking error under load startup of the (**a**) Control scheme of combining the backstepping controller with the ESO and (**b**) Control Scheme of combining the integral backstepping controller with the ELESO.

Figure 13 shows the d and q-axis currents of the two schemes under load startup. The higher harmonics are filtered out in Figure 13b, and the waveforms are smoother than those in Figure 13a. In addition, the currents in Figure 13b have a faster convergence speed and a smaller jump amplitude.

Figure 14 shows the speed-tracking waveforms of the two schemes under load startup. As shown in Figure 14a, the rotor speed reaches the set value of 0.4 s. The rotor can converge to the target speed after 0.2 s under the new system. Since high-frequency harmonics and other internal disturbances are filtered out, the speed can be stabilized at 1000 r/min thereafter. Therefore, the new system has good robustness.

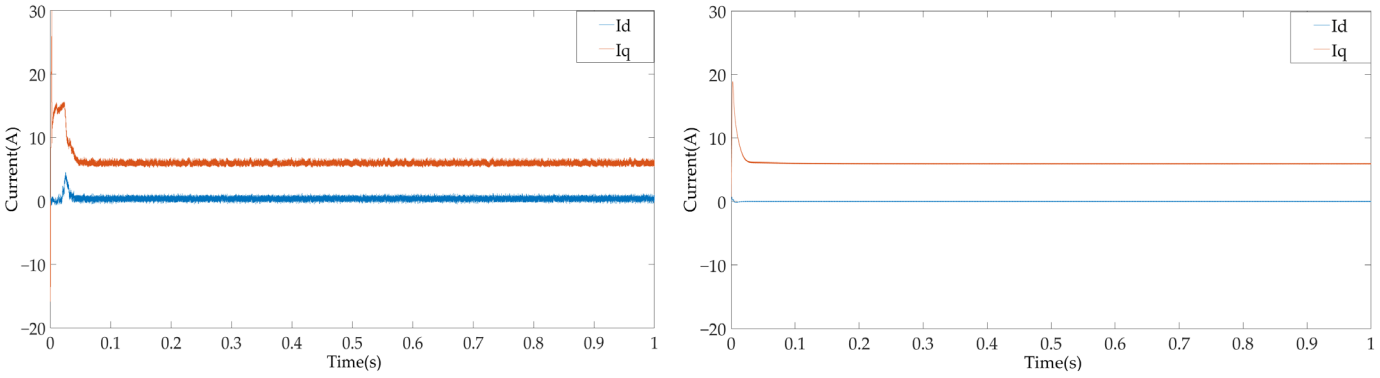

(**a**) (**b**)

Figure 13. PMSM d and q-axis currents under load startup of the (**a**) Control scheme of combining the backstepping controller with the ESO and (**b**) Control Scheme of combining the integral backstepping controller with the ELESO.

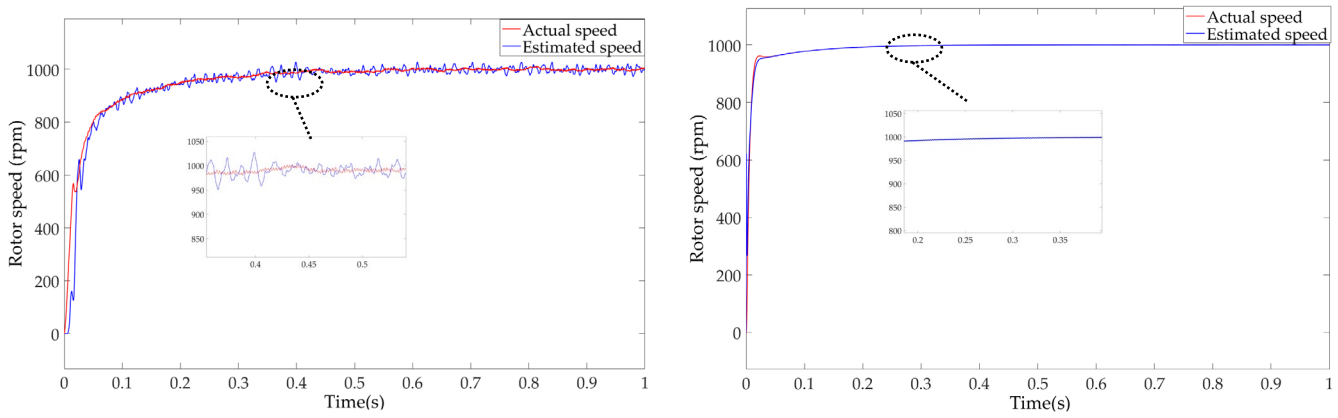

(**a**) (**b**)

Figure 14. PMSM rotor speed under load startup of the (**a**) Control scheme of combining the backstepping controller with the ESO and (**b**) Control Scheme of combining the integral backstepping controller with the ELESO.

According to the above experimental data, when the motor starts with load, the control scheme based on the combination of the backstepping controller and the ESO, as well as the control scheme based on the combination of the integral backstepping controller and the ELESO, will eventually produce a stable waveform. However, the control scheme based on the integral backstepping controller and the ELESO can accelerate to the rated speed faster in the startup phase, which is 0.2 s faster than the traditional control scheme. The control scheme combining the backstepping controller with the ESO still has a rotor estimation error of 0.2 rad when the system is stable. Due to the estimation of the internal disturbance of the system and the addition of integral terms to the backstepping controller, the control scheme based on the integral backstepping controller and the ELESO can obtain better static stability. Through no-load acceleration and on-load starting experiments, it is verified that the PMSM sensorless control system based on the integral backstepping controller and the ELESO has better performance and stronger robustness. The simulation results realize the PMSM high-precision control without a position sensor.

3.2. Experimental Results and Analysis

The feasibility of the control scheme based on the combination of the integral backstepping controller and the ELESO is preliminarily verified through simulation. On this basis, the motor test bench shown in Figure 3 is used for experimental verification. The

magnetic particle brake and tension controller provide load to the PMSM. The dynamic torque sensor can display the change of dynamic parameters such as speed and torque of the PMSM. At zero speed and low speed, the back EMF is very small, and the rotor position cannot be accurately estimated. I-F open-loop startup is usually used to cover the startup from standstill through the low-speed area. After rotor pre-positioning, the method applies a constant q-axis current to drag the speed up to the desired speed, then switches to a medium-high speed angle observer [36].

According to the simulation results, two experiments are designed to verify the superiority of the control scheme based on the integral backstepping controller and the ELESO. These experiments also use the control scheme based on the backstepping controller and the ESO as a comparison. Firstly, PMSM starts at no load and accelerates to 500 r/min. At 0.5 s, the PMSM accelerates to 1000 r/min. When the time reaches 1 s, the load jumps to 6 N·m. Finally, the load drops to 0 N·m at 1.5 s, and the PMSM keeps running at this state. Figure 15 shows the speed waveforms under this experiment. The total duration of the experiment is set to 2 s. The timeline of the experiment is marked in Figure 15, and all the following waveforms are based on this timeline. Figure 15 clearly shows that when the system state changes, the control scheme based on the integral backstepping controller and the ELESO has a faster response speed. Figure 16 shows the actual position and estimated position of the rotor after taking the remainder under the two schemes. In Figure 16, the errors of the two schemes are small, which will be difficult to show the superiority of the improved scheme. In this paper, the position and speed information are quantified in the table for a clearer comparison. Table 2 shows the estimated and actual values of position and speed under the two schemes. According to the design of experiment 1, the appropriate time points are selected for data acquisition. In experiment 1, after the PMSM is started, the system state changes three times at 0.5 s, 1 s and 1.5 s. Table 2 shows that the control scheme based on the integral backstepping controller and the ELESO has better tracking effect in the whole process of experiment 1. The rotor position tracking error is basically stable within 0.1 rad, which is greatly improved compared with the control scheme based on the backstepping controller and the ESO. When the system state changes, the rotor speed jump amplitude of the improved scheme is lower. Moreover, when the system operates stably, especially when the load value is rated, the steady-state error of the control scheme based on the integral backstepping controller and the ELESO is smaller, and its speed can converge to the set value faster.

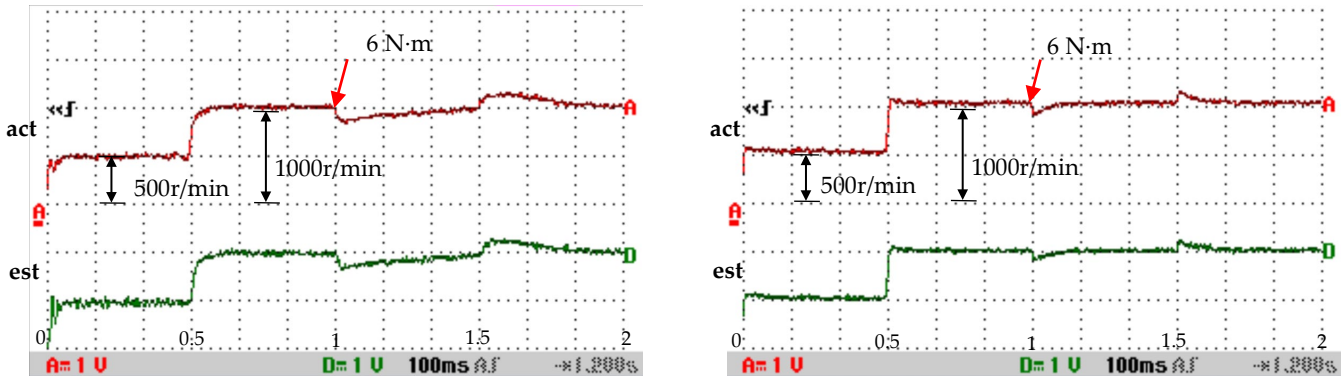

(**a**) (**b**)

Figure 15. Experiment 1 PMSM rotor speed waveforms of the (**a**) Control scheme of combining the backstepping controller with the ESO and (**b**) Control Scheme of combining the integral backstepping controller with the ELESO.

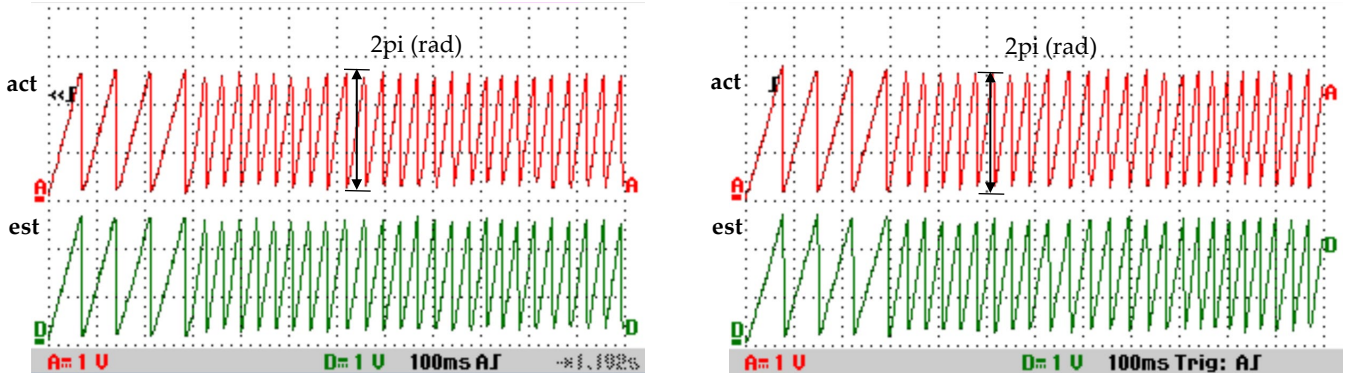

(**a**) (**b**)

Figure 16. Experiment 1 PMSM rotor position waveforms of the (**a**) Control scheme of combining the backstepping controller with the ESO and (**b**) Control Scheme of combining the integral backstepping controller with the ELESO.

Table 2. Position and speed of experiment 1.

Time (s)	Speed (a) Act/Est	Speed (a) Error	Speed (b) Act/Est	Speed (b) Error	Position (a) Act/Est	Position (a) Error	Position (b) Act/Est	Position (b) Error
0.01	363.85/137.69	226.16	500.45/501.5	−1.05	0.81/0.39	0.42	1.69/1.82	−0.13
0.05	470.00/462.84	7.16	506.67/505.13	1.54	2.16/1.48	0.68	4.52/4.61	−0.09
0.1	510.40/524.53	−14.13	503.87/502.75	1.12	1.72/1.13	0.59	4.45/4.51	−0.06
0.3	500.58/497.83	2.75	500.15/499.03	1.12	3.38/2.75	0.63	6.17/6.23	−0.06
0.55	960.06/979.30	−19.24	1015.57/1013.61	1.96	1.35/0.5	0.85	5.80/5.88	−0.08
0.6	1007.67/1005.30	2.37	1003.86/1002.66	1.2	5.99/4.68	1.31	6.14/6.19	−0.05
0.8	1001.32/1006.70	−5.38	1000.29/999.41	0.88	5.28/4.09	1.19	4.14/4.18	−0.04
1.05	873.38/870.16	3.22	945.46/945.07	0.39	1.05/0.03	1.02	4.72/5.14	−0.42
1.1	926.43/921.41	5.02	995.04/994.04	1	1.43/0.3	1.13	2.05/2.44	−0.39
1.3	967.17/931.65	35.52	999.82/998.94	0.88	1.10/0.08	1.02	6.16/6.22	−0.06
1.55	1112.68/1140.04	−27.36	1056.01/1053.08	2.93	5.98/4.58	1.4	1.14/1.21	−0.07
1.6	1110.35/1107.98	2.37	1011.21/1010.24	0.97	2.79/1.39	1.4	1.44/1.48	−0.04
1.8	1042.10/1036.18	5.92	1000.99/1000.23	0.76	2.71/1.45	1.26	3.51/3.55	−0.04

Figure 17 is the current waveforms diagram of the d and q-axis. Figure 18 shows the electromagnetic torque waveforms. In Figure 17, both schemes have obtained stable current waveforms. However, the jump amplitude of the q-axis current in Figure 17b is smaller when the speed changes. Figure 18a shows that the waveform jitter with internal interference (higher harmonics) will be very obvious. In high performance control occasions, such control performance is not allowed. The reference value of d-axis current is always 0. According to the time point selected in Table 2, the d-axis currents and electromagnetic torques are quantized in Table 3. Comparing the data of the two schemes, the d-axis current error and electromagnetic torque error of the control scheme based on the integral backstepping controller and the ELESO are 1–10% of the error of the comparison scheme. The control scheme based on the integral backstepping controller and the ELESO shows better control performance.

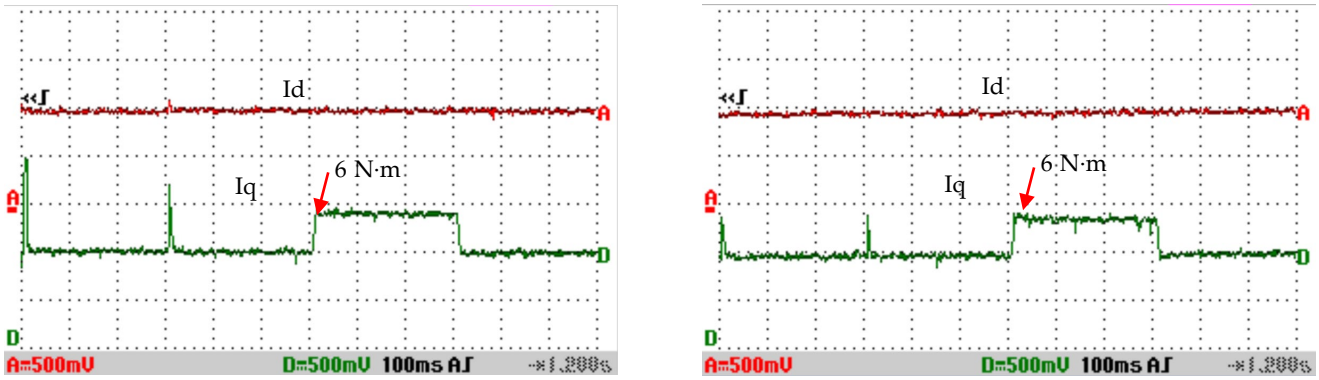

(**a**) (**b**)

Figure 17. Experiment 1 PMSM d and q-axis currents of the (**a**) Control scheme of combining the backstepping controller with the ESO and (**b**) Control Scheme of combining the integral backstepping controller with the ELESO.

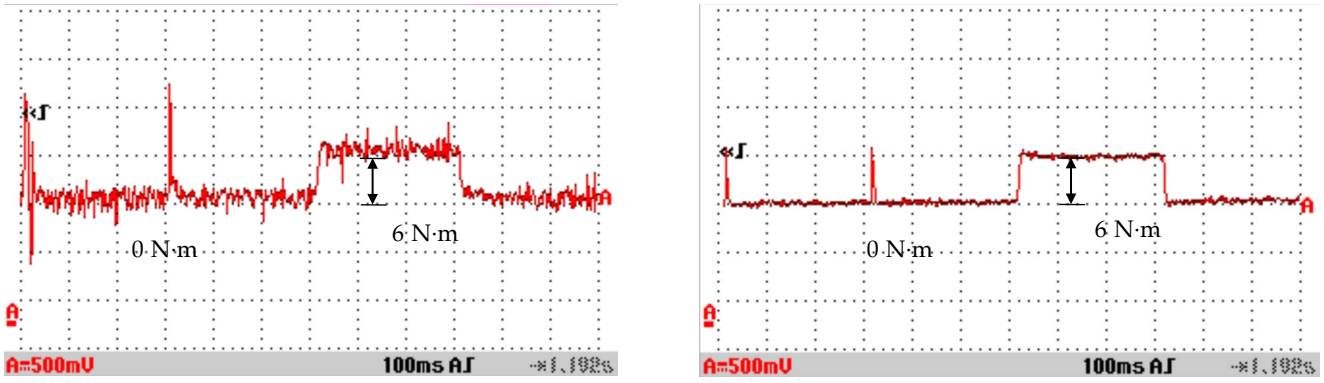

(**a**) (**b**)

Figure 18. Experiment 1 PMSM electromagnetic torque waveforms of the (**a**) Control scheme of combining the backstepping controller with the ESO and (**b**) Control Scheme of combining the integral backstepping controller with the ELESO.

Table 3. D-axis current and torque of experiment 1.

Time (s)	Id (a)	Id (b)	Torque (a)	Torque (b)
0.01	1.20	0.05	9.84	1.31
0.05	−0.27	−0.003	2.12	0.04
0.1	0.16	−0.002	0.78	0.03
0.3	−0.023	0.001	−0.60	0.01
0.55	0.50	0.002	−2.16	−0.04
0.6	0.013	−0.001	−1.57	−0.01
0.8	0.72	−0.002	2.02	0
1.05	0.60	−0.01	6.03	6.21
1.1	0.25	0.003	7.49	6.08
1.3	0.09	0.002	6.32	6.01
1.55	0.39	0.006	1.68	−0.19
1.6	0.62	0	0.64	−0.09
1.8	0.22	−0.003	0.81	−0.01

The load startup and speed jump test of PMSM are also essential steps to verify its sensorless control performance. Experiment 2 is designed as PMSM load startup and speed

jump experiment. PMSM starts at the set value of 1000 r/min and 6 N·m. Then, the speed jumps to 800 r/min at 1 s.

Figure 19 shows the speed waveforms of Experiment 2. Figure 20 shows the estimated value and actual value of the rotor position after taking the remainder. Similar to experiment 1, the relevant parameters in Figures 19 and 20 are quantified in Table 4. According to the data in Table 4, the speed in Figure 19b can reach the set value in only 0.3 s, which is much faster than the waveform in Figure 19a. Moreover, in Figure 19b, when the speed reaches the set value, PMSM can operate stably at the set value, and the steady-state error is close to 0. During the whole control process, the rotor position estimation error shown in Figure 20b is always stable around 0.4 rad. Comparing with Figure 20a, the estimation error is reduced to 30–40%.

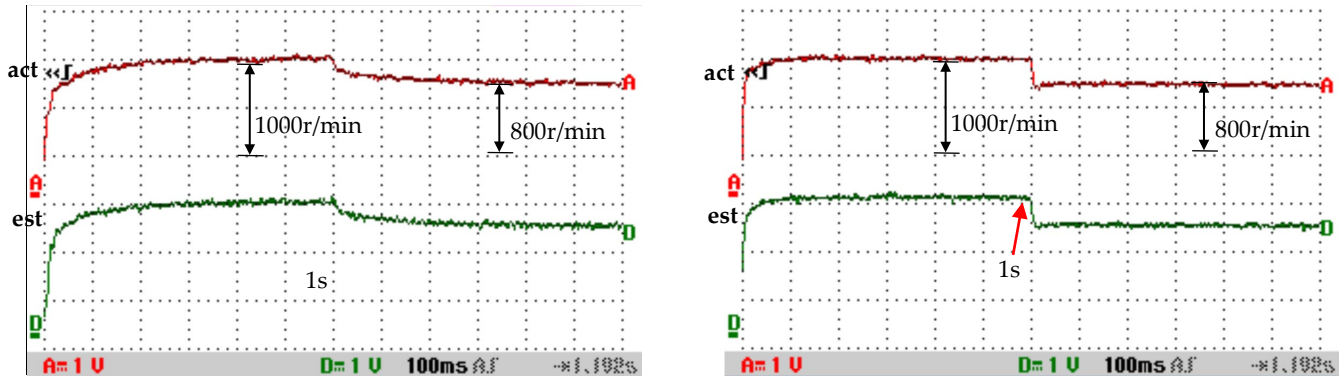

(**a**) (**b**)

Figure 19. Experiment 2 PMSM rotor speed waveforms of the (**a**) Control scheme of combining the backstepping controller with the ESO and (**b**) Control Scheme of combining the integral backstepping controller with the ELESO.

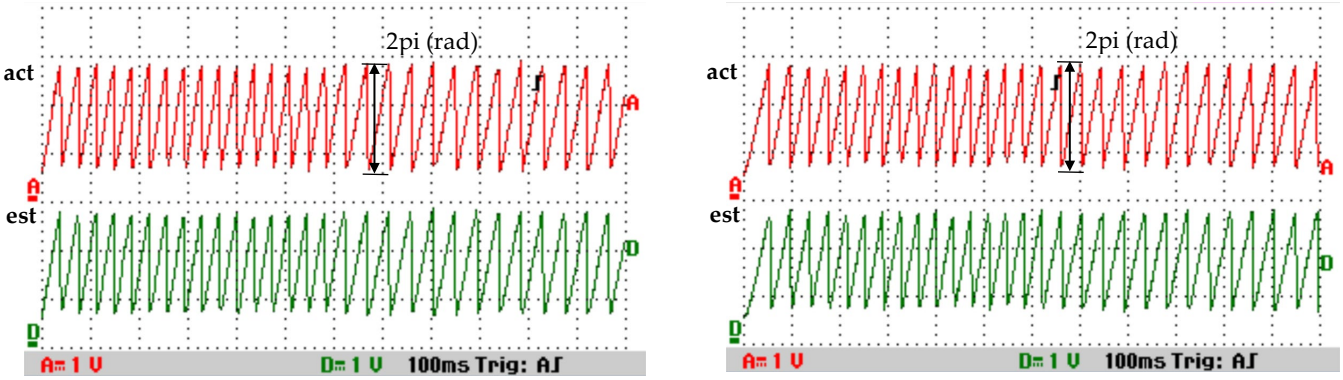

(**a**) (**b**)

Figure 20. Experiment 2 PMSM rotor position waveforms of the (**a**) Control scheme of combining the backstepping controller with the ESO and (**b**) Control Scheme of combining the integral backstepping controller with the ELESO.

Table 4. Position and speed of experiment 2.

Time (s)	Speed (a) Act/Est	Speed (a) Error	Speed (b) Act/Est	Speed (b) Error	Position (a) Act/Est	Position (a) Error	Position (b) Act/Est	Position (b) Error
0.1	812.50/814.99	−2.49	965.98/964.67	1.31	5.51/4.49	1.02	4.76/5.16	−0.4
0.3	939.87/947.73	−7.86	998.68/997.78	0.9	6.23/5.13	1.1	6.01/6.24	−0.23
0.5	970.27/987.90	−17.63	999.97/999.06	0.91	2.18/0.98	1.2	1.79/2.18	−0.39
0.7	985.96/987.44	−1.48	1000.01/999.11	0.9	1.34/0.08	1.24	3.89/4.28	−0.39
0.9	993.17/1010.23	−17.06	1000.02/999.08	0.9	1.30/0.03	1.27	5.81/6.20	−0.39
1.1	859.71/858.22	1.49	795.70/794.77	0.93	4.73/3.61	1.12	5.83/6.27	−0.44
1.3	822.55/803.84	18.71	799.83/798.87	0.96	1.13/0.2	0.93	3.70/4.14	−0.44
1.5	808.29/802.55	5.74	799.98/799.03	0.95	1.04/0.02	1.02	1.60/2.04	−0.44
1.7	799.04/803.83	−4.79	799.99/799.03	0.96	5.95/4.99	0.96	5.80/6.23	−0.43
1.9	805.53/780.67	24.86	799.99/799.02	0.97	4.05/3.04	1.01	3.70/4.14	−0.44

Figure 21 shows the current waveforms of d and q-axis under experiment 2. In Figure 21a, when the rotor speed changes, the current waveforms have a very obvious jump. Moreover, due to the existence of higher harmonics, the electromagnetic torque waveform in Figure 22a has a large fluctuation. In Figure 22b, higher harmonics are filtered, and the waveform is smoother. Table 5 shows the d-axis currents and torques data of the two schemes in Experiment 2. According to the data in Table 5, the steady-state error of d-axis current in Figure 21b is 0.001–0.002. The electromagnetic torque error in Figure 22b is stable at 0.01. Experiment 2 proves that the control scheme based on the integral backstepping controller and the ELESO has a faster response speed, lower parameters jump and smaller steady-state errors when starting and changing speed under the constant load. This is consistent with the results of experiment 1.

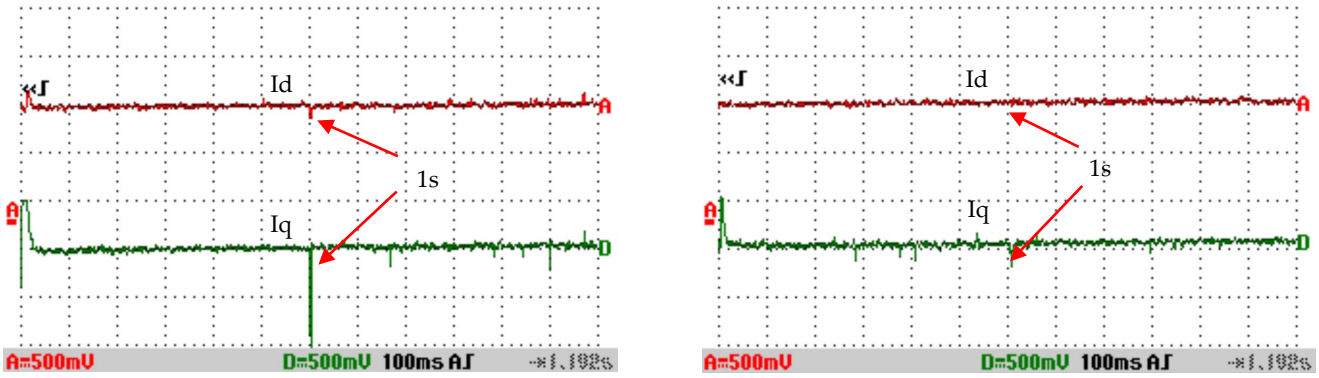

(**a**) (**b**)

Figure 21. Experiment 2 PMSM d and q-axis currents of the (**a**) Control scheme of combining the backstepping controller with the ESO and (**b**) Control Scheme of combining the integral backstepping controller with the ELESO.

In conclusion, the above experiments further verify that the control scheme based on the integral backstepping controller and the ELESO has better performance than the scheme based on the backstepping controller and the ESO. The experimental results show that the simulation results are correct. Compared with the ESO, the ELESO eliminates the interference of the higher harmonics. The backstepping controller can greatly reduce the influence of the parameter changes and the charge disturbances by introducing the integral action in each step to ensure high accuracy speed control. The scheme can be applied to places with high performance.

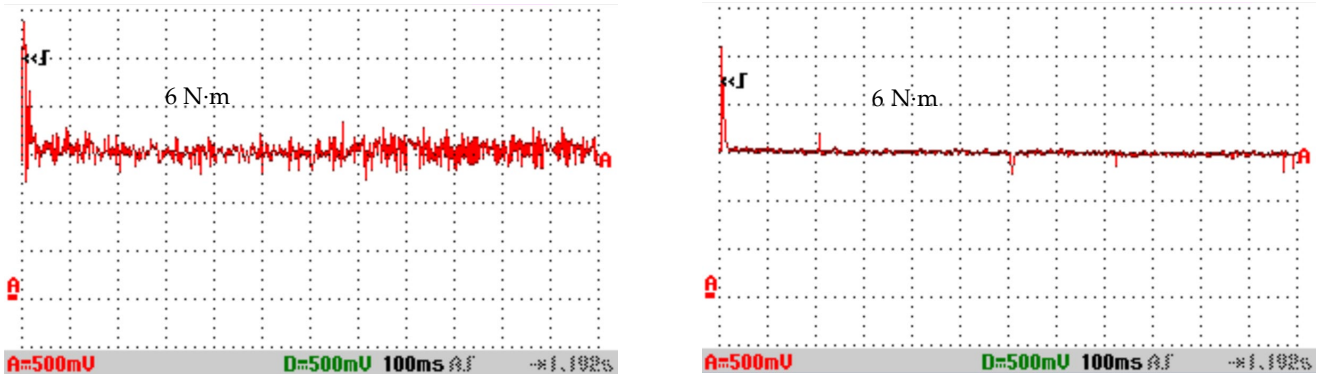

(**a**) (**b**)

Figure 22. Experiment 2 PMSM electromagnetic torque waveforms of the (**a**) Control scheme of combining the backstepping controller with the ESO and (**b**) Control Scheme of combining the integral backstepping controller with the ELESO.

Table 5. D-axis current and torque of experiment 2.

Time (s)	Id (a)	Id (b)	Torque (a)	Torque (b)
0.1	0.35	−0.002	8.84	6.06
0.3	0.50	0.002	8.49	6.02
0.5	−0.013	0.002	6.39	6.01
0.7	0.28	0.002	6	6
0.9	0.132	0.002	6.72	6.01
1.1	−0.15	0.002	3.68	6.04
1.3	−0.011	−0.001	6.57	6.01
1.5	−0.12	−0.001	6.07	6
1.7	−0.36	−0.001	4.74	6
1.9	−0.05	0	5.34	6.01

4. Conclusions

According to the characteristics of the sensorless control system, this paper proposes a sensorless control scheme that combines the integral backstepping controller with the ELESO to improve the performance of the system.

The LESO proposed by the control algorithm has the advantage of estimating the system disturbance without requiring an accurate motor model. On this basis, the algorithm improves the performance of the sensorless system by cascading another new LESO to estimate and compensate for the sixth harmonic component. Moreover, the control system provides the integral speed backstepping controller with the estimation value of the rotor speed obtained by the ELESO. The q-axis current reference value is obtained by designing a Lyapunov function. The current reference values in the synchronous rotating coordinate system are transferred to the integral current backstepping controllers to obtain the d and q-axis voltages. The reference voltages and the estimated rotor position obtained by the ELESO are transmitted to the SVPWM to realize the whole FOC sensorless control process. The acceleration and load startup experiments are carried out on the control model to verify that the improved algorithm has a faster convergence speed and more accurate position estimation. In addition, the control algorithm can effectively eliminate motor chattering and phase delay, which has good stability under static and dynamic conditions. The simulation results show that the PMSM sensorless control system based on the integral backstepping controller and the ELESO is effective and has good load interference suppression capability.

Author Contributions: Conceptualization, L.S. and C.Z.; methodology, L.S. and C.Z.; software, Y.Z. and G.X.; validation, L.S., C.Z., G.X. and X.H.; formal analysis, X.H.; resources, L.S.; data curation, C.Z.; writing—original draft preparation, C.Z.; writing—review and editing, L.S., X.Z., Y.Z. and G.X. All authors have read and agreed to the published version of the manuscript.

Funding: This research was funded by Basic Public Welfare Research Program of Zhejiang (Yanjuan Qin: LGG19F010010).

Institutional Review Board Statement: Not applicable.

Informed Consent Statement: Not applicable.

Data Availability Statement: The research data used and/or analyzed during the current study are available from the corresponding author on reasonable request.

Conflicts of Interest: The authors declare no conflict of interest.

References

1. Zhao, N.; Wang, G.; Xu, D.; Zhu, L.; Zhang, G.; Huo, J. Inverter Power Control Based on DC-Link Voltage Regulation for IPMSM Drives without Electrolytic Capacitors. *IEEE Trans. Power Electron.* **2018**, *33*, 558–571. [CrossRef]
2. Zhao, Y.; Wei, C.; Zhang, Z.; Qiao, W. A Review on Position/Speed Sensorless Control for Permanent-Magnet Synchronous Machine-Based Wind Energy Conversion Systems. *IEEE J. Emerg. Sel. Top. Power Electron.* **2013**, *1*, 203–216. [CrossRef]
3. Kim, S.-Y.; Choi, C.; Lee, K.; Lee, W. An Improved Rotor Position Estimation with Vector-Tracking Observer in PMSM Drives with Low-Resolution Hall-Effect Sensors. *IEEE Trans. Ind. Electron.* **2010**, *58*, 4078–4086. [CrossRef]
4. Liu, Y.; Zhu, J.; Wang, Z.; Liang, Y. Study of rotor position estimation algorithm based on back-EMF voltage for dual-winding fault-tolerant permanent magnet motor. *Automatika* **2022**, *63*, 496–510. [CrossRef]
5. Kim, J.; Jeong, I.; Nam, K.; Yang, J.; Hwang, T. Sensorless Control of PMSM in a High-Speed Region Considering Iron Loss. *IEEE Trans. Ind. Electron.* **2015**, *62*, 6151–6159. [CrossRef]
6. Xu, W.; Jiang, Y.; Mu, C.; Blaabjerg, F. Improved Nonlinear Flux Observer-Based Second-Order SOIFO for PMSM Sensorless Control. *IEEE Trans. Power Electron.* **2019**, *34*, 565–579. [CrossRef]
7. Qiao, Z.; Shi, T.; Wang, Y.; Yan, Y.; Xia, C.; He, X. New Sliding-Mode Observer for Position Sensorless Control of Permanent-Magnet Synchronous Motor. *IEEE Trans. Ind. Electron.* **2013**, *60*, 710–719. [CrossRef]
8. Liang, D.; Li, J.; Qu, R.; Kong, W. Adaptive Second-Order Sliding-Mode Observer for PMSM Sensorless Control Considering VSI Nonlinearity. *IEEE Trans. Power Electron.* **2018**, *33*, 8994–9004. [CrossRef]
9. Ren, N.; Fan, L.; Zhang, Z. Sensorless PMSM Control with Sliding Mode Observer Based on Sigmoid Function. *J. Electr. Eng. Technol.* **2021**, *16*, 933–939. [CrossRef]
10. Fu, D.; Zhao, X.; Zhu, J. A Novel Robust Super-Twisting Nonsingular Terminal Sliding Mode Controller for Permanent Magnet Linear Synchronous Motors. *IEEE Trans. Power Electron.* **2021**, *37*, 2936–2945. [CrossRef]
11. Xiang, L.; Yan, W.; Zhicheng, J. Global Fast Terminal Sliding Mode Control System for Permanent Magnet Synchronous Motor Drive Under Disturbances. In Proceedings of the 2018 37th Chinese Control Conference (CCC), Wuhan, China, 25–27 July 2018; pp. 3092–3095. [CrossRef]
12. Nguyen, T.H.; Nguyen, T.T.; Nguyen, V.Q.; Le, K.M.; Tran, H.N.; Jeon, J.W. An Adaptive Sliding-Mode Controller with a Modified Reduced-Order Proportional Integral Observer for Speed Regulation of a Permanent Magnet Synchronous Motor. *IEEE Trans. Ind. Electron.* **2022**, *69*, 7181–7191. [CrossRef]
13. Lu, E.; Li, W.; Wang, S.; Zhang, W.; Luo, C. Disturbance rejection control for PMSM using integral sliding mode based composite nonlinear feedback control with load observer. *ISA Trans.* **2021**, *116*, 203–217. [CrossRef]
14. Li, Z.; Wang, J.; Wang, S.; Feng, S.; Zhu, Y.; Sun, H. Design of Sensorless Speed Control System for Permanent Magnet Linear Synchronous Motor Based on Fuzzy Super-Twisted Sliding Mode Observer. *Electronics* **2022**, *11*, 1394. [CrossRef]
15. Xiong, J.-J.; Zhang, G.-B.; Wang, J.-X.; Yan, T.-H. Improved Sliding Mode Control for Finite-Time Synchronization of Nonidentical Delayed Recurrent Neural Networks. *IEEE Trans. Neural Netw. Learn. Syst.* **2020**, *31*, 2209–2216. [CrossRef]
16. Han, J. From PID to Active Disturbance Rejection Control. *IEEE Trans. Ind. Electron.* **2009**, *56*, 900–906. [CrossRef]
17. Qu, L.; Qiao, W.; Qu, L. An Extended-State-Observer-Based Sliding-Mode Speed Control for Permanent-Magnet Synchronous Motors. *IEEE J. Emerg. Sel. Top. Power Electron.* **2021**, *9*, 1605–1613. [CrossRef]
18. Du, B.; Wu, S.; Han, S.; Cui, S. Application of Linear Active Disturbance Rejection Controller for Sensorless Control of Internal Permanent-Magnet Synchronous Motor. *IEEE Trans. Ind. Electron.* **2016**, *63*, 3019–3027. [CrossRef]
19. Xi, Y.; Yu, X.; Wang, Y.; Li, Y.; Huang, J. Robust Nonlinear Adaptive Backstepping Coordinated Control for Boiler-Turbine Units. In Proceedings of the 2018 IEEE 27th International Symposium on Industrial Electronics (ISIE), Cairns, Australia, 13–15 June 2018; pp. 1167–1172. [CrossRef]
20. Nabipour, M.; Zarchi, H.A.; Madani, S.M. Variable-structure position control-a class of fast and robust controllers for synchronous reluctance motor drives. In Proceedings of the 20th Iranian Conference on Electrical Engineering (ICEE2012), Tehran, Iran, 15–17 May 2012; pp. 410–415. [CrossRef]

21. Xi, Y.; Wang, Y.A. Coordinated Control Strategy for Thermal Power Generation Units Based on the Adaptive Backstepping Method. *Zhongguo Dianji Gongcheng Xuebao* **2018**, *38*, 2070. [CrossRef]
22. Kang, Y.G.; Reigosa, D.D. Dq-Transformed Error and Current Sensing Error Effects on Self-Sensing Control. *IEEE J. Emerg. Sel. Top. Power Electron.* **2022**, *10*, 1935–1945. [CrossRef]
23. Humaidi, A.J.; Badr, H.M.; Ajil, A.R. Design of Active Disturbance Rejection Control for Single-Link Flexible Joint Robot Manipulator. In Proceedings of the 2018 22nd International Conference on System Theory, Control and Computing (ICSTCC), Sinaia, Romania, 10–12 October 2018; pp. 452–457. [CrossRef]
24. Jiang, F.; Yang, K.; Sun, S.; Xu, Y.; Liu, A. Back-EMF based Sensorless Control of PMSM with an Improved PLL for Eliminating the Position Estimation Fluctuation. In Proceedings of the 2019 22nd International Conference on Electrical Machines and Systems (ICEMS), Harbin, China, 11–14 August 2019. [CrossRef]
25. Wang, G.; Ding, L.; Li, Z.; Xu, J.; Zhang, G.; Zhan, H.; Ni, R.; Xu, D. Enhanced Position Observer Using Second-Order Generalized Integrator for Sensorless Interior Permanent Magnet Synchronous Motor Drives. *IEEE Trans. Energy Convers.* **2014**, *29*, 486–495. [CrossRef]
26. Jiang, F.; Yang, K.; Sun, S.; Zhang, H.; Tang, L.; Liu, A. An Improved Extended State Observer Based on Linear-Nonlinear Switching Strategy for PMSM Sensorless Control. In Proceedings of the 2018 21st International Conference on Electrical Machines and Systems (ICEMS), Jeju, Korea, 7–10 October 2018; pp. 1696–1702. [CrossRef]
27. Hua, X.; Huang, D.; Guo, S. Extended State Observer Based on ADRC of Linear System with Incipient Fault. *Int. J. Control. Autom. Syst.* **2020**, *18*, 1425–1434. [CrossRef]
28. Gao, Z. Scaling and bandwidth-parameterization based controller tuning. In Proceedings of the 2003 American Control Conference, Denver, CO, USA, 4–6 June 2003; pp. 4989–4996. [CrossRef]
29. Qu, L.; Qiao, W.; Qu, L. An Enhanced Linear Active Disturbance Rejection Rotor Position Sensorless Control for Permanent Magnet Synchronous Motors. *IEEE Trans. Power Electron.* **2020**, *35*, 6175–6184. [CrossRef]
30. Karabacak, M.; Eskikurt, H.I. Design, modelling and simulation of a new nonlinear and full adaptive backstepping speed tracking controller for uncertain PMSM. *Appl. Math. Model.* **2012**, *36*, 5199–5213. [CrossRef]
31. Larbaoui, A.; Belabbes, B.; Meroufel, A.; Tahour, A.; Bouguenna, D. Backstepping control with integral action of PMSM integrated according to the MRAS observer. *IOSR J. Electr. Electron. Eng.* **2014**, *9*, 59–69. [CrossRef]
32. Yang, Q.; Liu, W.; Huang, Y. Real time simulation study on backstepping sliding mode control of permanent magnet synchronous motor. In Proceedings of the 2011 International Conference on Electrical Machines and Systems (ICEMS), Beijing, China, 20–23 August 2011; pp. 1–5. [CrossRef]
33. Sun, X.; Yu, H.; Liu, X. Design and Application of Sliding Mode Controller in PMSM Position Tracking Control Based on Adaptive Backstepping. In Proceedings of the 2018 Chinese Automation Congress (CAC), Xi'an, China, 30 November 2018–2 December 2018; pp. 3507–3511. [CrossRef]
34. Nicola, C.-I.; Nicola, M.; Selișteanu, D. Sensorless Control of PMSM Based on Backstepping-PSO-Type Controller and ESO-Type Observer Using Real-Time Hardware. *Electronics* **2021**, *10*, 2080. [CrossRef]
35. Noguchi, S.; Mabuchi, H.; Suzuki, K.; Dohmaeki, H. Study of parameter variations compensation in sensorless control of PMSM. In Proceedings of the 2016 19th International Conference on Electrical Machines and Systems (ICEMS), Chiba, Japan, 13–16 November 2016; pp. 1–6.
36. Pacha, M.; Zossak, S. Improved Simple I-F Open-Loop Start-up of PMSM Drives without Speed or Position Sensor. In Proceedings of the 2019 IEEE 10th International Symposium on Sensorless Control for Electrical Drives (SLED), Turin, Italy, 9–10 September 2019; pp. 1–6. [CrossRef]